DEVELOPMENT OF THE T+M COUPLED FLOW-GEOMECHANICAL SIMULATOR TO DESCRIBE FRACTURE PROPAGATION AND COUPLED FLOW-THERMAL-GEOMECHANICAL PROCESSES IN TIGHT/SHALE GAS SYSTEMS

Jihoon Kim, George J. Moridis
Lawrence Berkeley National Laboratory
1 Cyclotron Rd.
Berkeley, CA, 94706, USA
e-mail: JihoonKim@lbl.gov

ABSTRACT

We developed a T+M hydraulic fracturing simulator by coupling a flow simulator with a geomechanics code. Modeling of the vertical fracture development involves continuous updating of the boundary conditions and of the connectivity data. This T+M simulator can model the initial fracture development during hydraulic fracturing operations, after which the domain description changes from single continuum to double or multiple continua, in order to rigorously model both flow and geomechanics. The T+H simulator allows explicit description of nonlinear permeability and geomechanical moduli, provides two-way coupling between fluid and heat flow and geomechanics, and continuously tracks changes in the fracture(s) and in the pore volume, and fully accounts for leak-off in all directions during hydraulic fracturing.

1. INTRODUCTION

Hydraulic fracturing is widely used in reservoir engineering applications to increase production by enhancing permeability. In particular, gas production in shale/tight gas reservoirs typically hinges on hydraulic fracturing because of the extremely low permeability of such reservoirs.

Several studies to develop algorithms for coupled simulation have been made in reservoir engineering. Ji et al. (2009) developed a numerical model for hydraulic fracturing, considering coupled flow and geomechanics, in which the algorithm is based on a dynamic update of the boundary condition along the fracture plane, fundamentally motivated by node splitting. In addition, Nassir et al. (2012) incorporated shear failure into a hydraulic fracturing model. Dean and Schmidt (2008) employed the same fracturing algorithm as Ji et al. (2009), while using different criteria for tensile failure. Fu et al. (2011) used the node-splitting method when material undergoes tensile failure. The method by Ji et al. (2009) exclusively considers vertical fracturing, but allows the fracturing algorithm to be implemented easily to the finite element method, changing the boundary conditions and data connectivity. Furthermore, it can easily couple flow and geomechanics, accounting for leak-off of the proppants to the reservoirs. On the other hand, Fu et al. (2011) developed a method that is not restricted to vertical fracturing, but using this method for 3D fracturing problems causes considerable complexity in code development, and modification of the data connectivity is also challenging compared to Ji et al.'s (2009) algorithm. Moreover, the Fu et al. (2011) method only allows flow along gridblocks, so the leak-off of proppants to gridblocks cannot properly be considered.

For the aforementioned issues related to hydraulic fracturing, we have developed an algorithm similar to that of Ji et al. (2009). We address shear failure by implementing the Drucker-Prager and Mohr-Coulomb models, considering coupled flow and geomechanics affecting pore volume and permeability for the multiple porosity model.

2. MATHEMATICAL FORMULATION

2.1. Governing Equation

Hydraulic fracturing requires the combined modeling of coupled fluid and heat flow and geomechanics. The governing equation for fluid flow is as follows.

$$\frac{d}{dt}\int_\Omega m^k d\Omega + \int_\Gamma \mathbf{f}^k \cdot \mathbf{n} d\Gamma = \int_\Omega q^k d\Omega \qquad , (1)$$

where superscript k indicates the fluid component. $d(\cdot)/dt$ refers to the time derivative of a physical quantity $(\cdot)$ relative to the motion of

the solid skeleton. m^k is the mass of component k. $\mathbf{f}^k$, and q^k are its flux and source terms on the domain Ω with boundary Γ, where $\mathbf{n}$ is the normal vector of the boundary.

The mass of component k is written as

$$m^k = \sum_J \phi S_J \rho_J X_J^k \ , \qquad (2)$$

where subscript *J* indicates fluid phases. ϕ is the true porosity, defined as the ratio of the pore volume to the bulk volume in the deformed configuration. S_J, ρ_J, and X_J^k are saturation and density of phase *J*, and the mass fraction of component k in phase *J*.

The mass flux term is obtained from

$$\mathbf{f}^k = \sum_J (\mathbf{w}_J^k + \mathbf{J}_J^k) \ , \qquad (3)$$

where $\mathbf{w}_J^k$ and $\mathbf{f}_J^k$ are the convective and diffusive mass flows of component *k* in phase *J*, respectively. For the liquid phase, *J*=*L*, $\mathbf{w}_J^k$ can be given by Darcy's law as

$$\mathbf{w}_J^k = X_J^k \mathbf{w}_J,$$
$$\mathbf{w}_J = -\frac{\rho_J k_{rJ}}{\mu_J}\mathbf{k}\left(\mathbf{Grad} p_J - \rho_J \mathbf{g}\right), \qquad (4)$$

where $\mathbf{k}$ is the absolute (intrinsic) permeability tensor. The terms μ_J, k_{rJ}, p_J are the viscosity, relative permeability, and pressure of the fluid phase *J*, respectively. $\mathbf{g}$ is the gravity vector, and $\mathbf{Grad}$ is the gradient operator. Note that, depending on the circumstances, other, more flow equations may be appropriate, such as the Forchheimer equation (Forchheimer, 1901) that incorporates laminar, inertial and turbulent effects.

For the gaseous phase, *J*=*G*, $\mathbf{w}_G^k$ is given by

$$\mathbf{w}_G^k = X_G^k \mathbf{w}_G$$
$$\mathbf{w}_G = -\left(1 + \frac{k_K}{P_G}\right)\frac{\rho_G k_{rG}}{\mu_G}\mathbf{k}\left(\mathbf{Grad} p_G - \rho_G \mathbf{g}\right) \qquad (5)$$

where k_K is the Klinkenberg factor. The diffusive flow can be written as

$$J_J^k = -\phi S_J \tau_G \rho_J \mathbf{D}_J^k \mathbf{Grad} X_J^k \ , \qquad (6)$$

where $\mathbf{D}_J^k$ and τ_G are the hydrodynamic dispersion tensor and gas tortuosity, respectively.

The governing equation for heat flow comes from heat balance, as

$$\frac{d}{dt}\int_\Omega m^H d\Omega + \int_\Gamma \mathbf{f}^H \cdot \mathbf{n} d\Gamma = \int_\Omega q^H d\Omega \ , \qquad (7)$$

where the superscript H indicates the heat component. m^H, $\mathbf{f}^H$, and q^H are heat, its flux, and source terms, respectively. The term m^H is the heat accumulation term, and is expressed as

$$m^H = (1-\phi)\int_{T_0}^{T} \rho_R C_R dT + \sum_J \phi S_J \rho_J e_J \ , \qquad (8)$$

where ρ_R, C_R, T, and T_0 are the density and heat capacity of the porous medium, temperature, and reference temperature, respectively. The heat flux is written as

$$\mathbf{f}^H = -\mathbf{K}_H \mathbf{Grad} T + \sum_J h_J \mathbf{w}_J \ , \qquad (9)$$

where $\mathbf{K}_H$ is the composite thermal conductivity tensor of the porous media. The specific internal energy, e_J, and enthalpy, h_J, of components *k* in phase *J* become, respectively

$$e_J = \sum_k X_J^k e_J^k \ , \ h_J = \sum_k X_J^k h_J^k \qquad (10)$$

The governing equation for geomechanics is based on the quasi-static assumption (Coussy 1995), written as

$$\mathbf{Div}\boldsymbol{\sigma} + \rho_b \mathbf{g} = \mathbf{0}, \qquad (11)$$

where $\mathbf{Div}$ is the divergence operator, $\boldsymbol{\sigma}$ is the total stress tensor, and ρ_b is the bulk density. The infinitesimal transformation is used to allow the strain tensor, $\boldsymbol{\varepsilon}$, to be the symmetric gradient of the displacement vector, $\mathbf{u}$,

$$\boldsymbol{\varepsilon} = \frac{1}{2}\left(\mathbf{Grad}^T \mathbf{u} + \mathbf{Grad}\,\mathbf{u}\right) \qquad (12)$$

where $\mathbf{Grad}$ is the gradient operator. The boundary conditions for the geomechanical problems are as follows; $\mathbf{u} = \bar{\mathbf{u}}$, given displacement, on a boundary Γ_u, and $\boldsymbol{\sigma}\cdot\mathbf{n} = \bar{\mathbf{t}}$, traction on a boundary Γ_t, where $\Gamma_u \bigcup \Gamma_t = \partial\Omega$, the

boundary over the domain, and $\Gamma_u \bigcap \Gamma_t = \emptyset$. The initial total stress satisfies the mechanical equilibrium with the boundary conditions. We may take a larger domain than a reservoir in order to determine geomechanics and heat transport more accurately.

Remark 1. Note that the boundary conditions for a given mathematical model in hydraulic fracturing are not prescribed but rather dependent on geomechanical solutions (i.e., nonlinearity). Conventional plastic mechanics, such as Mohr-Coulomb failure, results in material nonlinearity, while the boundary conditions are still prescribed (Simo and Hughes, 1998; Wang et al., 2004). On the other hand, the geomechanics of hydraulic tensile fracturing in this study does not yield material nonlinearity while nonlinearity lies in the boundary condition (Ji et al., 2009).

2.2. Constitutive relations

Gas flow within homogeneous rock can be modeled using single porosity poromechanics, extended from Biot's theory (Coussy, 1995). However, when failure occurs and fractures are created, we have local heterogeneity because fractures and rock matrix coexist. In this case, we use double or multiple porosity models, which allow local heterogeneity. In particular, for single phase flow, the constitutive equations are written as follows (Berryman, 2002, Kim et al., 2012).

$$\delta\boldsymbol{\sigma} = \overbrace{\mathbf{C}_{up}\delta\boldsymbol{\varepsilon}}^{\delta\boldsymbol{\sigma}'} - \sum_l b_l^* \delta p_l \mathbf{1} - \sum_l \widetilde{b}_l^* \delta T_l \mathbf{1}, \qquad (13)$$

$$b_l^* = -K_{dr} b_l,\ \widetilde{b}_l^* = -K_{dr}\widetilde{b}_l,$$

$$\delta\zeta_l = b_l^* \delta\varepsilon_v + \sum_m L_{l,m}^{-1}\delta p_m + \sum_m \overline{D}_{l,m}\delta T_m, \qquad (14)$$

where the subscript l indicates a material (subelement) within a gridblock. The terms K_{dr} and $\mathbf{C}_{up}$ are the upscaled elastoplastic drained bulk and tangent moduli at the level of the gridblock, respectively, and b_l^* and $\widetilde{b}_l^*$ are the coupling coefficients. b_l , $\widetilde{b}_l$, K_{dr}, $L_{l,m}^{-1}$ are written as

$$b_l = -\frac{\alpha_l \eta_l}{K_l},\ \widetilde{b}_l = -3\alpha_{T,l}\eta_l,$$

$$K_{dr} = \sum_l \frac{\eta_l}{K_l},\ \mathbf{L}^{-1} = \begin{bmatrix} \eta_f N_f & 0 \\ 0 & \eta_M N_M \end{bmatrix}, \qquad (15)$$

where α_l , $\alpha_{T,l}$, η_l , and K_l are the Biot coefficient, thermal dilation coefficient, volume fraction, and drained bulk modulus for material *l,* respectively. The term $L_{l,m}(\equiv \mathbf{L})$ represents the Biot modulus matrix of the double porosity model (e.g., the fracture-rock matrix system), where N_f and N_M are the inverse of the Biot moduli, M_f and M_M, for the fracture and rock matrix media, respectively, (i.e., $N_f = 1/M_f$ and $N_M = 1/M_M$). The subscripts f and M indicate the fracture and rock matrix. $\overline{D}_{l,m}$ is the coupling coefficient between fluid flow and heat flow.

For naturally fractured reservoirs, the double porosity model is used initially, while, in this study, we change the single porosity model into a double porosity during simulation when a material fails. Thus, for the naturally fractured reservoirs, $\mathbf{C}_{up}$ and K_{dr} on the level of a gridblock are obtained from an upscaling of given fracture and rock matrix material properties. The return mapping for elastoplasticity is performed at all the subelements (Kim et al., 2012).

On the other hand, in this study, $\mathbf{C}_{up}$ and K_{dr} are directly obtained from the elastoplastic tangent moduli at a gridblock (global) level, not the subelements, while we need to determine the drained bulk moduli of fracture and rock matrix materials for the double porosity model, followed by the coupling coefficients. To this end, we assume that the rock matrix has the same drained bulk modulus as that of the single porosity material before plasticity (i.e., elasticity), because the rock matrix is undamaged (Kim and Moridis, 2012a). Then, from Eq. 15_3, the drained bulk modulus of the fracture can be determined by

$$K_f = \eta_f \frac{K_{dr} K_M}{K_M - K_{dr}(1-\eta_f)}. \qquad (16)$$

Considering K_{dr} and K_f to be positive for well-posedness, the volume fraction of the fracture, η_f, has the constraint as

$$\eta_f > 1 - \frac{K_M}{K_{dr}}. \tag{17}$$

2.3. Failure and Fracturing

We consider two types of failure in geomaterials: tensile and shear failure.

2.3.1. Tensile failure

We use the tensile failure condition for large-scale fracture propagation, as follows.

$$\sigma'_n \geq T_c \ , \tag{18}$$

where σ'_n is the effective stress normal to the plane of a potential fracture, and T_c is the tensile strength of a material. The tensile strength is determined from a tension test such as the Brazilian test. For a given geomechanical loading, the boundary condition for geomechanics is modified when the tensile effective stress reaches the tensile failure condition. In other words, the internal natural (Neumann) boundary conditions are introduced at the areas where the tensile effective stress satisfies the condition of the tensile failure (Eq. 18).

Remark 2. The geomechanics status at early time when tensile fracturing occurs is assumed to exist in undrained condition, with the exception of adding surface loads at the boundary conditions (i.e., traction due to fracturing). The traction normal to the fracture surface, $\bar{t}_f$, can be determined as $\bar{t}_f = \bar{p}_f$. Here, at the early time, we set $\bar{p}_f$ to be the initial reservoir pressure, which implies that the pressure at the fracture is locally equilibrated with the surroundings. On the other hand, after the early time, $\bar{p}_f$ changes due to flow of the proppants.

2.3.2. Shear failure

For shear failure, we use the Drucker-Prager and Mohr-Coulomb models, which are widely used to model the failure of cohesive frictional materials. The Drucker-Prager model of this study is expressed as

$$\begin{aligned} f &= \beta_f I_1 + \sqrt{J_2} - \kappa_f \leq 0, \\ g &= \beta_g I_1 + \sqrt{J_2} - \kappa_g \leq 0, \end{aligned} \tag{19}$$

where I_1 is the first invariant of the effective stress and J_2 is the second invariant of the effective deviatoric stress. f and g are the yield and plastic potential functions, respectively. The Mohr-Coulomb model is given as

$$\begin{aligned} f &= \tau'_m - \sigma'_m \sin\Psi_f - c_h \cos\Psi_f \leq 0, \\ g &= \tau'_m - \sigma'_m \sin\Psi_d - c_h \cos\Psi_d \leq 0, \end{aligned} \tag{20}$$

$$\sigma'_m = \frac{\sigma'_1 + \sigma'_3}{2}, \ \tau'_m = \frac{\sigma'_1 - \sigma'_3}{2} \tag{21}$$

where $\sigma_1', \sigma_2', \sigma_3'$ are, respectively, the maximum, intermediate, and minimum principal effective stresses, where tensile stress is positive. Ψ_f and Ψ_d are the friction and dilation angles, respectively. c_h is the cohesion.

3. NUMERICAL MODELING

We developed the T+M hydraulic fracturing simulator by coupling the LBNL in-house simulator **T**OUGH+RealGasH2O (for the description of nonisothermal flow of water and real gas mixture through porous/fractured media) with the ROC**M**ECH in-house geomechanics simulator. Below, we describe the numerical algorithms and characteristics of the coupled simulator.

3.1. Discretization

Space discretization is based on the integral finite difference method (a finite volume technique) in the simulation of flow and heat flow (TOUGH+RealGasH2O code), and the finite element method in the geomechanical component of the coupled simulations (ROCMECH code). Time discretization in both constituent components of T+M is based on the standard backward method that is typically employed in reservoir simulations.

3.2. Failure Modeling

3.2.1. Tensile failure and node splitting

We introduce the new internal Neumann boundaries by splitting nodes, and assign the traction from the fluid pressure inside the fractures.

Node splitting is performed based on the physical tensile strength. In this study, the focus is on vertical tensile fracturing. Because of symmetry, we extend the numerical simulation capabilities to 3D domains. Then, the fracture plane is located at the outside boundary (Ji et al., 2009).

3.2.2. Shear failure and elastoplasticity

We use classical elastoplastic return-mapping algorithms for the Mohr-Coulomb and Drucker-Prager models (Simo and Hughes, 1998). Unlike for tensile fracturing, we account for shear failure with no assumption of a certain fracturing direction. The Drucker-Prager model provides a simple closed analytical formulation for return mapping because it is associated only with I_1 and J_2. However, the Mohr-Coulomb model also takes J_3, and thus the return mapping is not straightforward, as it is in the Drucker-Prager model.

For the Mohr-Coulomb model, we employ the two-stage return mapping algorithm proposed by Wang et al. (2004) after slight modifications. In the return mapping of the Mohr-Coulomb model at the edges of the failure envelope, we also employ the Drucker-Prager model with explicit treatment of J_3 to avoid numerical instability. According to Kim and Moridis (2012a), the adjusted Drucker-Prager model for the Mohr-Coulomb model (i.e., explicit treatment of J_3) can also simulate the Mohr-Coulomb failure accurately.

3.3. Sequential Implicit Approach

There are two typical methods for solving coupled problems: fully coupled and sequential implicit. The fully coupled method usually provides unconditional and convergent numerical solutions for mathematically well-posed problems. The price for these important advantages is that it requires a unified flow-geomechanics simulation, which results in enormous software development effort and large computational costs.

On the other hand, the sequential implicit method uses existing simulators for the solution of the constituent subproblems. For example, the problem of nonisothermal flow, or of geomechanics, is solved implicitly, fixing certain geomechanical (or flow) variables, and then geomechanics (or flow) is solved implicitly from the flow/geomechanics variables obtained from the previous step. According to Kim et al. (2011), the fixed stress sequential scheme provides unconditional stability and numerical convergence with high accuracy. Using the fixed-stress split method, we can solve the flow problem, fixing the total stress field. This scheme can easily be implemented in flow simulators by using the Lagrange's porosity function and correction term, as follows.

$$\Delta\Phi_l^n = \left(\frac{\alpha_l^2}{K_l^n} + \frac{\alpha_l - \Phi_l^n}{K_s}\right) p_l^n + 3\alpha_{T,l}\alpha_l \Delta T_l^n - \frac{b_l}{\eta_l}\Delta\sigma_v^{n-1} \tag{22}$$

where $\Delta(\cdot)^n = (\cdot)^{n+1} - (\cdot)^n$. σ_v is the total volumetric mean stress. Φ is defined as the ratio of the pore volume in the deformed configuration to the bulk volume in the reference (initial) configuration. The porosity correction term, $b_l / \eta_l \Delta\sigma_v^{n-1}$, is calculated from geomechanics, which corrects the porosity estimated from the pore compressibility.

For permeability of the fracture, we use the following nonlinear permeability motivated by the cubic law.

$$k_{p,f} = k_{p,f}^0 \left(\frac{\omega}{\omega_0}\right)^{n_p}, \tag{23}$$

where $k_{p,f}$ and ω are the fracture permeability and its width, respectively. $k_{p,f}^0$ is a reference fracture permeability for a reference width ω_0. n_p characterizes the nonlinear fracture permeability. When $n_p = 3.0$, Eq. 23 is identical to the cubic law.

For Young's modulus of the fracture, we use a much low value, compared with the rock matrix, when tensile fracturing occurs. For shear failure, the return mapping algorithm automatically determines geomechanical properties such as Eq. 16.

4. NUMERICAL EXAMPLES

Here we first show a verification test, and then discuss a numerical example of hydraulic fracturing induced in a shale gas reservoir. A detailed discussion of this problem can be found in Kim and Moridis (2012b).

4.1. Verification

We use an analytical solution proposed by Sneddon and Lowengrud (1969) that can calculate the width of a fracture in 2D plane stain mechanics (Figure 1), written as

$$w = \frac{l}{E'}\int_0^1 p(sl,t)G_p(\frac{x}{l},s)ds,$$

$$G_p(\xi,s) = -\frac{4}{\pi}\ln\left|\frac{\sqrt{1-\xi^2}+\sqrt{1-s^2}}{\sqrt{1-\xi^2}-\sqrt{1-s^2}}\right|,$$

$$E' = \frac{E}{1-\nu^2}, \qquad (24)$$

where $p = p_f - \sigma_o$. E, and ν are Young's modulus and Poisson's ratio, respectively, p_f and σ_o are fluid pressure within the fracture and total stress normal to the fracture plane, respectively. x/l is the normalized distance from the reference point within the fracture, as shown in Figure 2. Figure 2 shows that the numerical solution matches the analytical solution, validating the simulator.

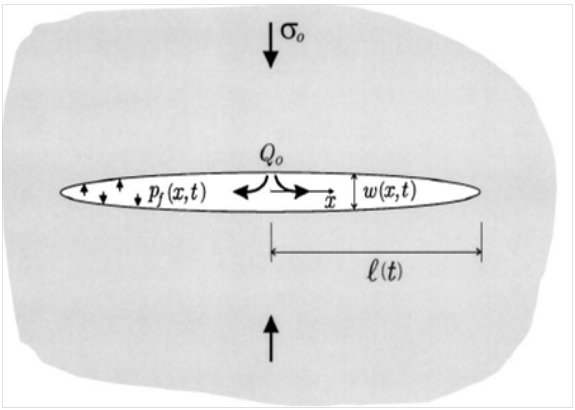

Figure 1. Schematics of a fracture in the 2D plane stain mechanics (Detournay, 2004)

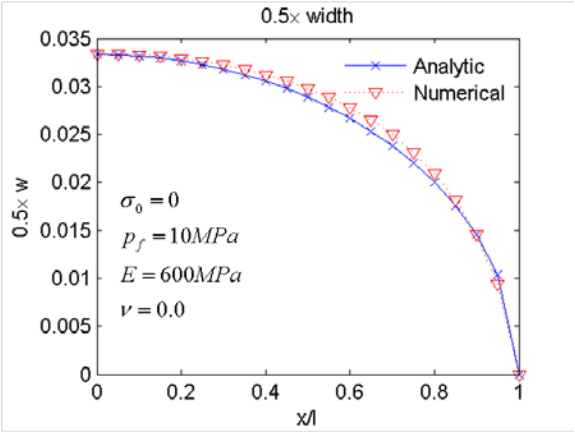

Figure 2. Comparison between the analytical and numerical solutions. The numerical solution matched the analytical solution.

4.2. 3D vertical fracture propagation

We assume the fracturing fluid to be water. We consider 3D coupled flow and geomechanical problems with constant injection rate. The geomechanical domain has 50, 5, 50 gridblocks in the x, y and z directions, respectively, with the x-z plane normal to the minimum compressive principal total stress. Gridblock sizes are uniform, i.e., Δx = Δz = 3 m in the x and z directions, respectively. The size of the gridblocks in the y direction is non-uniform; 0.1 m, 0.5 m 3.0 m, 10.0 m, 20.0 m.

Young's modulus and Poisson's ratio are 6 GPa and 0.3, respectively. The tensile strength of material for the reference case is 4.0 MPa. Initial fluid pressure is 17.10 MPa at 1350 m in depth with the 12.44 kPa/m gradient. Initial temperature is 58.75 ^{o}C at 1350 m in depth with the 0.025 ^{o}C/m gradient. Initial total principal stresses are -26.21 MPa, and -23.30 MPa, and -29.12 MPa at 1350 m depth in x, y, z directions, respectively, where the corresponding stress gradients are -19.42 kPa/m, -17.59 kPa/m, and -21.57 kPa/m, respectively. We set gravity based on a bulk density of 2200 kg/m^3, with no horizontal displacement boundary conditions at the sides (except at the fracture nodes), and no displacement boundary at the bottom.

For flow, we have, respectively, 50, 6, and 50 gridblocks in x, y, and z directions, where one more layer for the fracture plane is introduced for flow within the fracture. The initial permea-

bility and porosity of the shale reservoir are $8.648\times10^{-19}m^2 = 8.76\times10^{-7}$ Darcy, and 0.1. For tensile failure, the fracture permeability is determined from Eq. 23, where $k^0_{p,f} = 5.9\times10^{-11}m^2$ (60 Darcy), $\omega_0 = 1.0\times10^3 m$, and $n_p = 3.0$. For shear failure, we use a constant permeability, $5.9\times10^{-14}m^2$ (60 mD). Once failure occurs, we change the single porosity to the double porosity model where fracture and rock matrix volume fractions are 0.1 and 0.9. The reference fracture porosity is 0.9, when the fracture is created, and the porosity varies after the creation due to poromechanical effects. Biot's coefficient is 1.0. We specify a constant injection rate of 8.0kg/s at x=25 m, z=-1440 m.

Figure 3 shows the fracture propagation during hydraulic fracturing. At the initial time, we have small fracturing. After the initial fracturing, the fracture propagates and becomes larger because of proppant injection within the fracture, which induces additional geomechanical loading to the fracture surface, followed by fracturing.

We then perform another numerical test, in which $\Psi_f = \Psi_d = 28.6^0$ and $c_h = 2.0$ MPa, for shear failure as well as tensile failure. From Figure 4 (and comparing it to Figure 3), we find that shear failure limits the fracture propagation in vertical direction. Shear failure propagates horizontally, and the overall failure occurs not only vertically but also horizontally. Flow of the proppants to the horizontal direction is substantial, compared to the case without shear failure, because shear failure also increases permeability considerably.

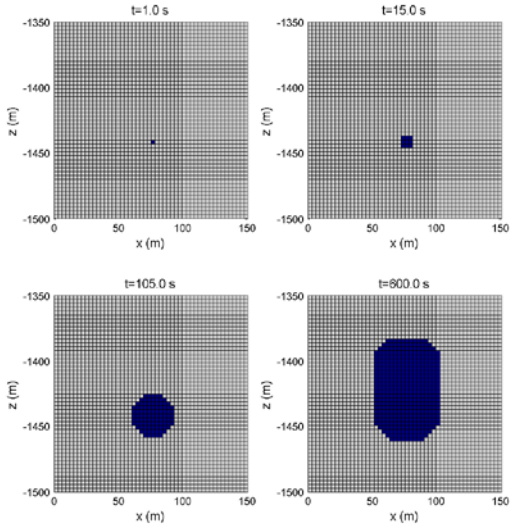

Figure. 3. Fracture propagation from tensile failure with of the constant injection rate of 8.0kg/s at x=25 m, z=-1440 m. The fracture propagation is stable and can be controlled by injection time.

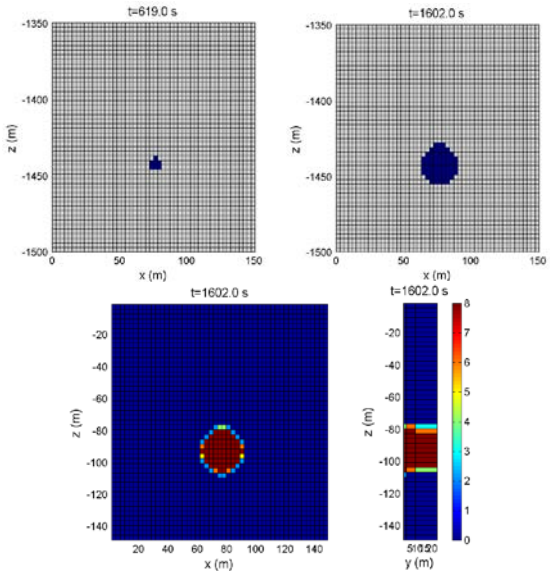

Figure. 4. Fracture propagation with $\Psi_f = \Psi_d = 28.6^0$ and $c_h = 2.0$ MPa. Top: the vertical fracture propagation due to tensile failure. Bottom: the areas of shear failure, where the number indicates failed Gauss points. Shear failure proceeds more horizontally, limiting the vertical fracture propagation.

SUMMARY

We developed the T+M hydraulic fracturing simulator by coupling the TOUGH+RealGasH2O flow simulator with the

ROCMECH geomechanics code. T+M has the following characteristics: (1) vertical fracturing is mainly modeled by updating the boundary conditions and the corresponding data structure; (2) shear failure can also be modeled during the fracturing; (3) a double- or multiple-porosity approach is employed after the initiation of fracturing in order to rigorously model flow and geomechanics; (4) nonlinear models for permeability and geomechanical properties can be easily implemented; (5) leak-off in all directions during hydraulic fracturing is fully considered; and (6) the code provides two-way coupling between fluid-heat flow and geomechanics, rigorously describing changes in the fractures, pore volumes, and permeabilities.

ACKNOWLEDGMENT

The research described in this article has been funded by the U.S. Environmental Protection Agency through Interagency Agreement (DW-89-92235901-C) to the Lawrence Berkeley National Laboratory, and by the Research Partnership to Secure Energy for America (RPSEA - Contract No. 08122-45) through the Ultra-Deepwater and Unconventional Natural Gas and Other Petroleum Resources Research and Development Program as authorized by the US Energy Policy Act (EPAct) of 2005. The views expressed in this article are those of the author(s) and do not necessarily reflect the views or policies of the EPA.

REFERENCES

Berryman JG. 2002. Extension of poroelastic analysis to double-porosity materials: New technique in microgeomechanics. *J. Eng. Mech. ASCE*; 128(8):840 – 847.

Coussy O. 1995. *Mechanics of porous continua*. Chichester, England: John Wiley and Sons.

Dean, R.H. and Schmidt, J.H., 2008 Hydraulic fracture predictions with a fully coupled geomechanical reservoir simulation. *SPE Annual Technical Conference and Exhibition*, Denver, Colorado, 21 – 24 Sep.

Detournay E. 2004. Propagation regimes of fluid-driven fractures in impermeable rocks *Int. J. Geomech*. 4(1) 35-45.

Forchheimer, P. 1901 Wasserbewegung durch Bode, *ZVDI*(1901), 45.

Fu P., and Johnson S.M., and Hao Y., and Carrigan C.R. 2011. Fully coupled geomechanics and discrete flow network modeling of hydraulic fracturing for geothermal applications. *6th workshop Geoth. Res. Eng.* 31 Jan.-2 Feb., Stanford, CA.

Ji, L., Settari A., Sullivan, R.B. 2009. A novel hydraulic fracturing model fully coupled with geomechanics and reservoir simulation. *Soc. Pet. Eng. J.*423-430.

Kim J., Tchelepi H.A., and Juanes R. 2011. Stability and convergence of sequential methods for coupled flow and geomechanics: Fixed-stress and fixed-strain splits. *Comput. Methods Appl. Mech. Engrg.* 200: 1591–1606.

Kim J., Sonnenthal E., and Rutqvist J. 2012. Formulation and sequential numerical algorithms of coupled fluid/heat flow and geomechanics for multiple porosity materials. *Int. J. Numer. Meth. Engrg.* In press, doi: 10.1002/nme.4340.

Kim J. and Moridis G. M. 2012a. Gas flow tightly coupled to elastoplastic geomechanics for tight and shale gas reservoirs: material failure and enhanced permeability. *SPE Uncon. Resour. Conf.*, Pittsburgh, PA, 5-7 Jun.

Kim J. and Moridis G. M. 2012b. Analysis of Fracture Propagation During Hydraulic Fracturing Operations in Tight/Shale Gas Systems, in prep.

Nassir M. and Settari A. and Wan R. 2012. Prediction and optimization of fracturing in tight gas and shale using a coupled geomechancial model of combined tensile and shear fracturing. *Hydr. Frac. Tech. Conf.* The woodland, TX, 6 – 8 Feb.

Simo, J.C. and Hughes, T.J.R. 1998. *Computational Inelasticity*. Heidelberg, Germany: Springer.

Sneddon, I., and Lowengrub, M. 1969. *Crack problems in the classical theory of elasticity*, Wiley, New York.

Wang X. and Wang L.B. and Xu L.M. 2004. Formulation of the return mapping algorithm for elastoplastic soil models. *Comput. Geotech.* **31**:315–338.